ON THE EFFECT OF INFRARED CAMERA POSITIONING FOR IN-FLIGHT BOUNDARY LAYER TRANSITION MEASUREMENTS

Christoph Mertens, Christoph.Mertens@nlr.nl, Royal Netherlands Aerospace Centre (NL)
Alberto F. Rius-Vidales, A.F.RiusVidales@tudelft.nl, Delft University of Technology (NL)
Marios Kotsonis, M.Kotsonis@tudelft.nl, Delft University of Technology (NL)
Henk Jentink, Henk.Jentink@nlr.nl, Royal Netherlands Aerospace Centre (NL)

Abstract

Infrared thermography is an optical measurement technique that is attractive for in-flight measurements of the boundary layer transition location on aircraft wings because it requires minimal instrumentation of the test object. A known drawback of this technique is however that the position of the infrared camera with respect to the analysed surface can influence the measurement accuracy. The positioning of the infrared camera on the test aircraft for in-flight measurements is a complex design trade-off that is influenced by many different factors. In this paper, measurement results from a wind tunnel experiment where adverse infrared camera positions were emulated are presented. Relatively simple corrections for the perspective distortion and the directional emissivity effects were subsequently applied to the image data. The results show that the boundary layer transition location can be extracted accurately and reliably under relatively steep viewing angles, with up until 75 degrees between the principal viewing axis and the surface normal direction. These results are useful for the design of in-flight experiments, where the demonstrated feasible range limit for the orientation between the infrared camera and the test surface can be used as a design constraint.

1. INTRODUCTION

The capability to perform accurate measurements of laminar-to-turbulent boundary layer transition (BLT) in free-flight conditions is crucial for advancing aircraft aerodynamic design and improving aircraft performance predictions. This capability is particularly relevant within the context of the aviation industry's shift towards sustainability, where delaying BLT to turbulence through innovative flow control technologies is of high interest due to its potential for increasing an aircraft's fuel efficiency by decreasing its friction drag [1]. These novel technologies, typically developed and validated in numerical simulations and wind tunnel experiments, must ultimately demonstrate their effectiveness in flight to progress toward commercial implementation.

Infrared thermography (IRT) has emerged as a leading technique for BLT detection in flight testing due to its non-intrusive nature and the associated minimal aircraft modification requirements. By capturing surface temperature distributions, IRT enables the efficient identification of the BLT location without the need for complex sensor instrumentation on the test aircraft. Because BLT significantly increases not only the friction drag but proportionally also the convective heat exchange, the BLT location can be extracted along the entire wingspan within the camera view by analyzing the behavior of the chordwise temperature gradient [2]. Many published studies employing IRT in free-flight scenarios have demonstrated its value in such applications, for example in Refs. [3-9].

However, while the underlying principles of IRT for BLT are well-established across laboratory and flight environments, the constraints on the infrared camera measurements in free-flight experiments pose unique challenges. One challenge is that the flight environment is less controlled than the wind tunnel environment with respect to temperature control and heat exchange. In the past, surfaces were often electrically heated to increase the heat exchange difference between the turbulent boundary layer and the laminar boundary layer. Nowadays, with more sensitive, modern infrared cameras, this is not strictly necessary any more [4]. Another consideration is that when the infrared camera is located in the cabin, then aircraft must be equipped with a special window which allows transmission in the infrared wavelength spectrum captured by the camera. Aircraft modifications for the flight test must be minimized to ensure cost-effective implementation, potentially forcing compromises in camera positioning with respect to the test object that significantly deviate from the ideal scenario (i.e. perpendicular to the wing surface) as it can be typically achieved in wind tunnel experiments, and, as a result, can degrade the image quality and complicate the data interpretation.

This paper addresses the effects of varying the infrared camera position with respect to the test object for in-flight BLT measurements. The study is performed based on a series of infrared images acquired in a controlled wind tunnel experiment with a rectangular unswept wing, where the orientation of the infrared camera with respect to the model is varied in a controlled manner. The objective is to define the parameter space for optimal and minimally acceptable camera orientation configurations during flight tests. These findings aim to simplify the design of in-flight IRT

experiments by providing clear guidelines, thereby enhance the reliability and efficiency of in-flight BLT measurement methodologies, which supports future advancements in aerodynamic research and sustainable aircraft design.

2. EXPERIMENTAL SETUP AND PROCEDURES

2.1 NLR Aeroacoustics Wind Tunnel

The wind tunnel experiment was conducted in the Aeroacoustics Wind Tunnel (AWT) at the Royal Netherlands Aerospace Centre facilities in Marknesse, Netherlands. The AWT is a 1:10 downscaled version of the DNW Large Low-Speed Facility, engineered for the cost-effective examination of technologies prior to their implementation in industrial-scale test campaigns. The AWT has a modular design, supporting both open and closed test section configurations and with various test section dimensions. For tests involving the open test section configuration, the facility is equipped with an anechoic chamber.

The present investigation used the closed test section configuration with a cross-sectional dimension of $950\text{mm} \times 950\text{mm}$, which at a freestream velocity of $U_\infty = 20\,\text{m/s}$ exhibits a turbulence intensity of around 0.01% which increases with increasing U_∞. For this particular experiment, the AWT was operated at a freestream velocity setting of $U_\infty = 28\,\text{m/s}$. However, one side wall of the closed test section has been removed to mount the optical measurement setup (see section 2.3). It can be expected that this modification introduces a change in the actual inflow velocity and angles experienced by the wing model, and an increase in turbulence intensity during the experiment, which is however of no further concern for the purpose of this study. The AWT was temperature-controlled to maintain a constant flow temperature of $T_\infty = 15°\text{C}$ during the experiment.

2.2 DLR-F15 Airfoil Wing Model

The investigated wing model is a rectangular, unswept wing that is made from aluminum, which features a modified version of the DLR-F15 airfoil. This multi-element airfoil was originally designed to be representative of large modern transport aircraft for conducting high-lift studies [10], as such it can be set in different high-lift configurations by installing a flap and slat at different angles. The modified DLR-F15 features a solid nose piece to replace the nose piece with slat. The trailing edge flap was fixed in the retracted position, resulting in the cross-sectional geometry shown in Figure 1.

The airfoil model has a stowed chord length of $c = 240\text{mm}$, which results in a chord-based Reynolds number of around 460,000 for this experiment, based on the set value for U_∞. To achieve an idealized two-dimensional flow condition, the model was mounted vertically on a turntable allowing to set the angle of attack α. With a span width of $s = 950\ \text{mm}$, the model spanned the entire test section width of the wind tunnel. For this experiment, two different angles of attack were tested, $\alpha = 4°$ and $\alpha = 5.5°$. Note that these are geometrically defined angles, the actual inflow angles are likely to differ due to the asymmetric test setup with one wind tunnel side wall removed.

Due to a lack of reference data, a brief analysis of this modified airfoil's performance is presented in the following, which has been conducted using the XFOIL software [11]. Figure 2 shows both the lift coefficient C_ℓ and boundary layer transition location x_{tr} on the suction surface of the airfoil over the varying angle of attack α. The Reynolds number has been set to 460,000 and the critical amplification ratio [12] has been set to $N = 12$ to approximate the conditions in the AWT. The lift curve increases nearly linearly from small negative values of α up until stall onset at $\alpha = 9°$, reaching $C_{\ell,\text{max}}$ at $\alpha = 10°$, before flow separation causes the lift to decrease for higher α. Small viscous effects on the lift slope are also visible around $\alpha = 4°$ as deviation from the ideal linear, inviscid lift slope. As visible in the transition polar, these effects are related to the upstream movement of the boundary layer transition location x_{tr}, showing a relatively steep change from near the trailing edge to near the leading edge between $\alpha = 2°$ and $\alpha = 5°$. The transitional boundary layer on the suction side of the airfoil in the α-region, where x_{tr} changes rapidly, is analyzed in more detail in the following.

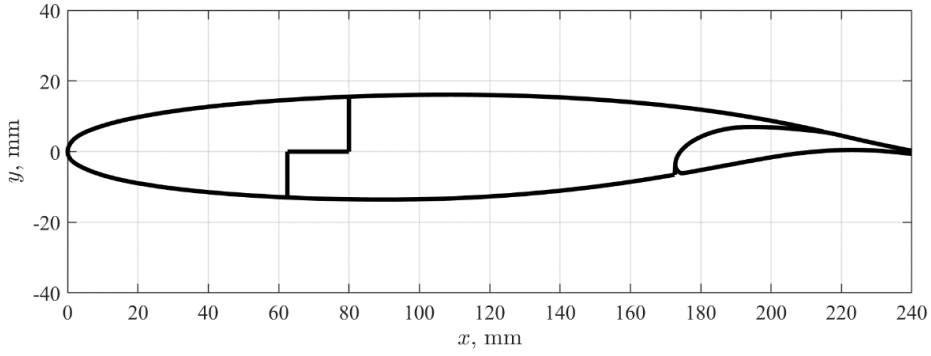

Figure 1: Modified DLR-F15 cross-sectional geometry.

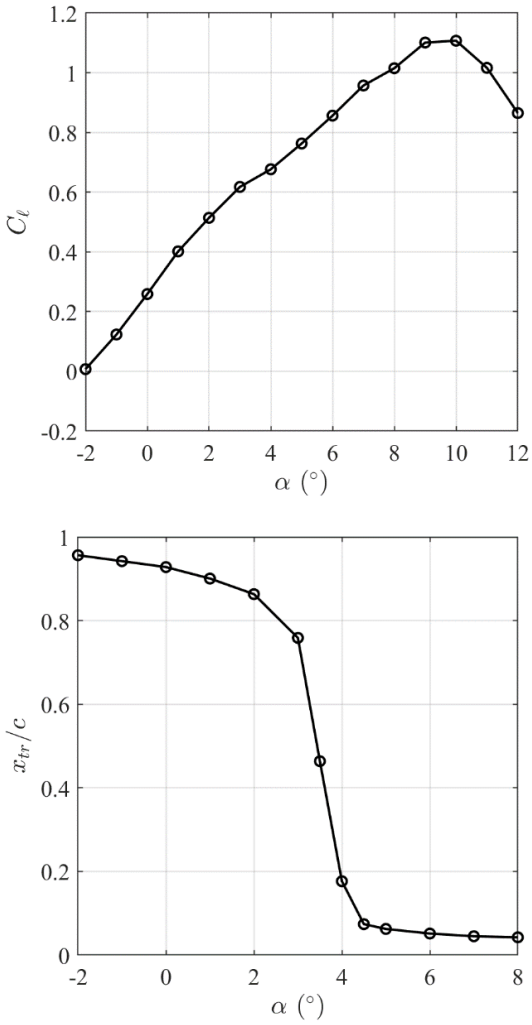

Figure 2: Results of the modified DLR-F15 airfoil analysis at Re = 460,000 performed using XFOIL. Top: lift coefficient polar. Bottom: suction side boundary layer transition location polar.

Figure 3 shows the local skin friction coefficient (C_f) distribution along the chord for three angles of attack in the mentioned α-region where x_{tr} moves rapidly upstream. At $\alpha = 3.5°$, the boundary layer flow remains laminar until approximately mid-chord, where transition to turbulence occurs at $x_{tr}/c = 0.46$. A small kink in the C_f-distribution near $x/c = 0.05$ is visible in all three curves and therefore likely an artifact of the geometry representation in XFOIL. For $\alpha = 4°$, the BLT location moves upstream to $x_{tr}/c = 0.18$, in this case the aforementioned kink causes C_f to become negative locally which is however not associated with BLT . As the angle of attack is increased to $\alpha = 4.5°$, laminar flow separation occurs near the leading edge, remaining separated until BLT occurs, which leads to turbulent reattachment, thus forming a short laminar separation bubble (LSB).

No direct quantitative agreement between the presented XFOIL results and the results of the experimental study discussed in this paper is expected, due to both the relatively low complexity of the boundary layer modelling employed in XFOIL and the differences in the actual experimental conditions in the wind tunnel. However, a qualitative agreement can be assumed regarding the flow topology at similar values of x_{tr}/c.

In the experiment, transition occurs near mid-chord for $\alpha_1 = 4°$, suggesting that the flow remains fully attached here. For $\alpha_2 = 5.5°$, transition occurs around $x/c = 0.15$, which is in same the region as the XFOIL results for $\alpha = 4.0°$ and $\alpha = 4.5°$, indicating the occurrence of flow separation and possibly BLT over a LSB in this experimental test case in the wind tunnel. For the experimental analysis of the BLT location, this differences are not further taken into account for this study.

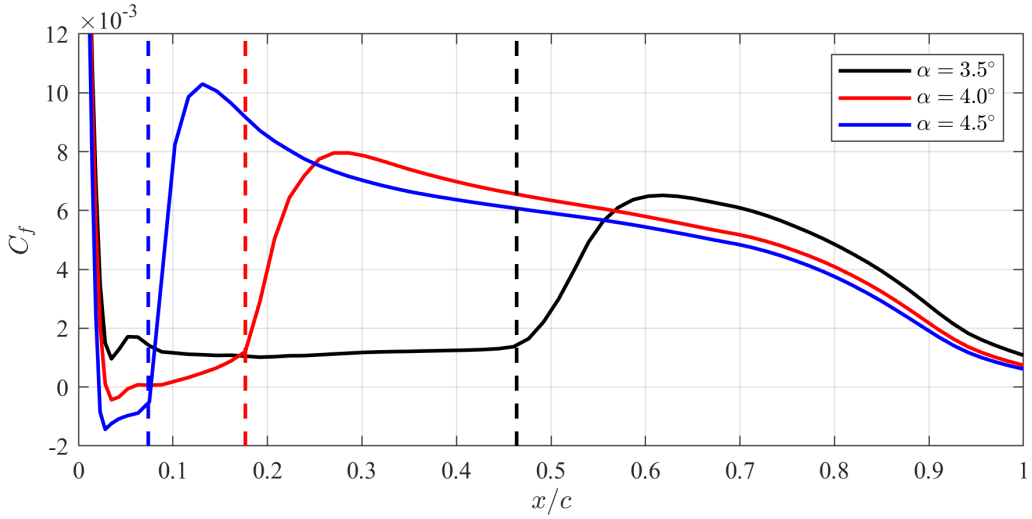

Figure 3: Skin friction distributions on the suction side of the modified DLR-F15 for various angles of attack. Vertical dashed lines indicate the boundary layer transition location as defined in XFOIL.

2.3 Infrared Camera Measurement Procedures

The IRT measurements are conducted with a FLIR® A655sc long-wave infrared camera, featuring a spectral range of $7.5–14.0\mu m$ and a sensor resolution of 640×480 pixels. The noise-equivalent temperature difference is reported to be below $30\ mK$ by the manufacturer [13]. Since the value of the local surface temperature is of no direct interest, image data is recorded without the use of a temperature calibration, thus measuring the raw camera intensity counts. This approach is sufficient for the temperature gradient-based BLT location determination and circumvents performing custom temperature calibrations [14].

The camera is mounted on a vertical aluminium stand, such that the camera lens is at the same vertical height as the centre of the wing model, viewing the suction side of the airfoil. The acrylic wind tunnel side wall must be removed because it is visually transparent but not transparent in the infrared waveband. The vertical stand is attached onto a metal plate that was manufactured to facilitate the positioning of the camera at 10 different orientation angles, all at a constant distance of $1m$ from the wing centre. The orientation is defined by the viewing angle, measured between the principal viewing axis of the camera and the surface normal direction. The viewing angle is varied between $0°$ (looking perpendicular at the wing) and a maximum of $85°$ (looking upstream from the trailing edge), first in $15°$ and then in $10°$ and $5°$ increments. Two different camera positions are shown on the photos from the wind tunnel experiment in Figure 5. The variation of the orientation along this single axis in the horizontal plane can be seen as worst-case scenario for IRT measurements, especially when the BLT location is near the leading edge of the wing. A movement of the camera in the vertical plane is expected to have a much smaller impact on the BLT measurements, since the curvature of the airfoil does not affect the result during such a variation. This means that the selected test case is best suited to extract relevant key learnings.

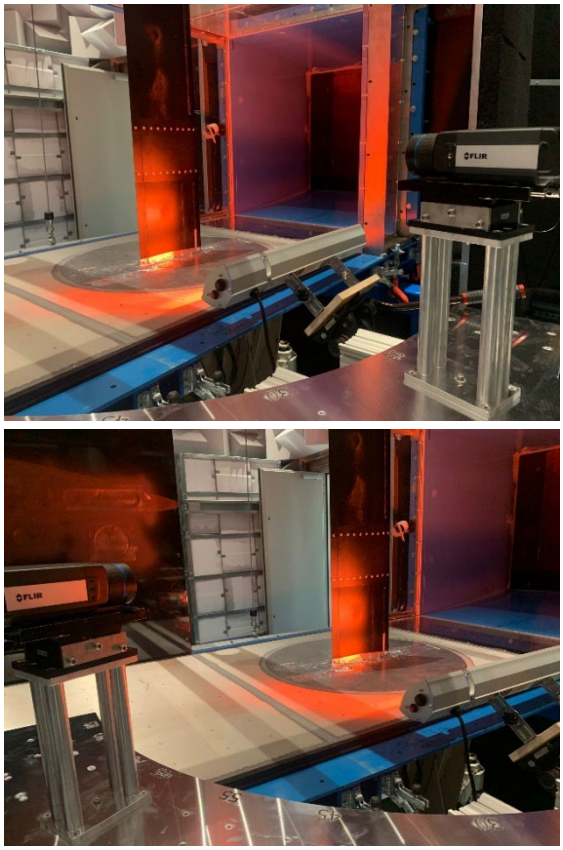

Figure 4: Measurement setup in the wind tunnel, view of the airfoil suction side, flow from right to left. Top: camera placement at viewing angle 15º. Bottom: camera placement at viewing angle 65º.

Also visible in the photos in Figure 5 is the heat lamp (2kW power output), which was mounted in a fixed position next to the wing to establish a temperature difference between the wing surface and the air flow, which is needed to perform the BLT measurements. The exact temperature increase produced by the heat lamp has not been measured but is estimated to be around $10℃$.

For the experiment, an approximately $200mm$ wide section of the wing model is wrapped along the entire chord length with a matte black vinyl foil, for enhancing thermal contrast in the infrared images. This wrapped section is equipped with 20 circular silver sticker markers at its spanwise edges. Each sticker has a diameter of $8mm$ and the stickers are distributed evenly along the chordwise direction. This level of surface modification to improve the thermal image quality and facilitate the perspective correction is similar to what can be done in preparation for flight tests.

The measurement procedure has been as follows: first, the heat lamp is switched on to heat up the wing model. Secondly, the wind tunnel is set to $U_\infty = 28\ m/s$. When the set velocity is reached, the live images from the infrared camera are observed for the surface temperature to drop until a thermal equilibrium is reached. Then, a series of 100 images is recorded for each test case and subsequently time-averaged per pixel to further reduce the random noise in the image.

It should be noted here that the multi-element airfoil wind tunnel model is far from ideal for performing IRT BLT measurements. The three different elements with gaps in between (and different surface treatments in the case of the flap) produce measurement artifacts in the infrared images (see section 3.1). However, such a less-than-ideal test object is representative of the adverse measurement conditions that can also be expected when conducting in-flight measurements on actual aircraft wings. As such, the measurements conducted on this model provide a relevant dataset considering the context of the purpose of this study.

3. DATA ANALYSIS

3.1 Perspective Correction

The first step in the data analysis of the time-averaged infrared images is the perspective correction. Changing the viewing angle of the infrared camera modifies the perspective with which the surface is imaged. This means that per pixel, a different area of the surface is imaged. In a ground testing setting, this correction can be achieved in different ways, considering that the shape of the test object and the relative positioning are both known (or can easily be determined) exactly. However, this is not representative of a flight test environment, where for example wing flexibility can introduce uncertainty in both wing shape and relative positioning.

A common, robust approach to the perspective correction is the use of surface markers that are easily detectable in the images. In the case of infrared measurements, fiducial markers must be used, having different thermal properties than the rest of the surface, such as the silver markers used in this study. These appear as cold spots in the infrared image, because they reflect the background temperature (see Figure 6).

Many different computational marker detection algorithms exist that automatically return the marker centroid locations in the image coordinate system. Because of the limited number of test cases in this study (20 images), the marker detection was performed manually. Once the marker positions are available, given that the physical locations of the markers on the object are already known, the perspective correction can be applied. Also for this processing step, many automated algorithms exist, in this study the "imwarp"-function that is implemented in MATLAB® was used, after first generating the image transformation with "fitgeotform2d" based on the marker locations. This function returns the perspective corrected images as shown exemplary for $65°$ in Figure 6.

In the following processing step, the image data is converted to one-dimensional data sets by taking the spanwise average along the central section of the wing between the markers, spanning 250 pixels. This step aims to further reduce the noise in the data and is justified by the expected two-dimensionality of the flow around the unswept an untapered wing model, which can also be verified in the images shown in Figure 6.

The previous processing steps did not account for the curved surface of the imaged object. Overall, the effect of this is not expected to be relevant for most the wing surface, particularly not in the region

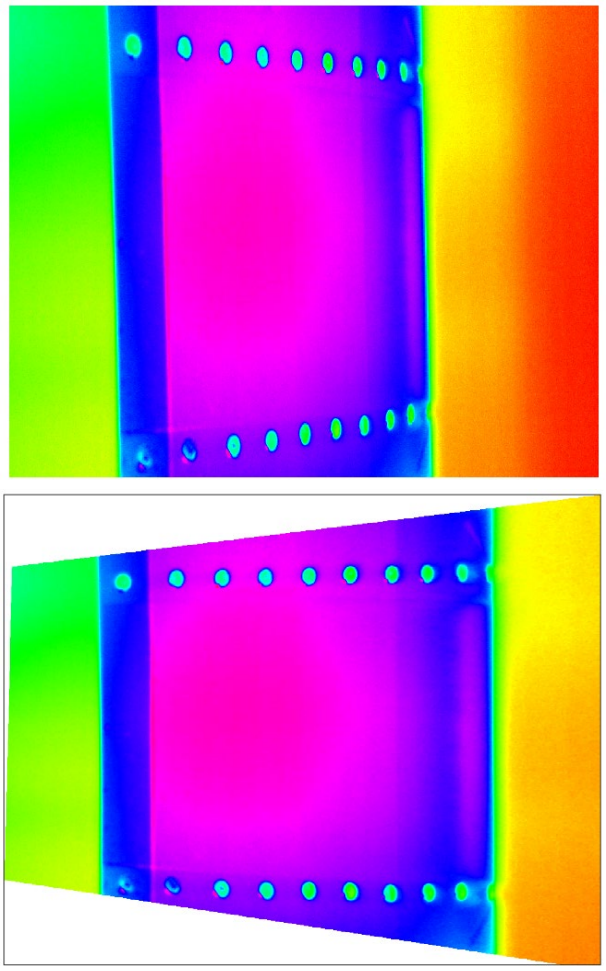

Figure 6: Example perspective correction for the infrared image at viewing angle 65º. Top: original image, bottom: perspective-corrected image.

far away from the edges. However, for ensuring the correct visualization of the one-dimensional data set, the image data is mapped to the airfoil chord length using a simple linear interpolation and extrapolation with the MATLAB® function "interp1". The interpolation is achieved making use of the fiducial markers again, this time in the already perspective-corrected images.

The results shown in Figure 7 are the temporal and spanwise-averaged radiation intensities measured with the infrared camera for the 10 different viewing angles, with the airfoil under an angle of attack of $4°$ and $5.5°$. Notably are the slightly varying overall temperature levels due to differences in the wind tunnel running time, the temperature drop towards the leading edge for the higher viewing angles due to the directional emissivity effects, as well as the measurement artifacts that occur at the junctions of the separate wing segments around $x/c = 0.35$ and $x/c = 0.9$.

The performed data processing steps until here form a practical approach to converting the image

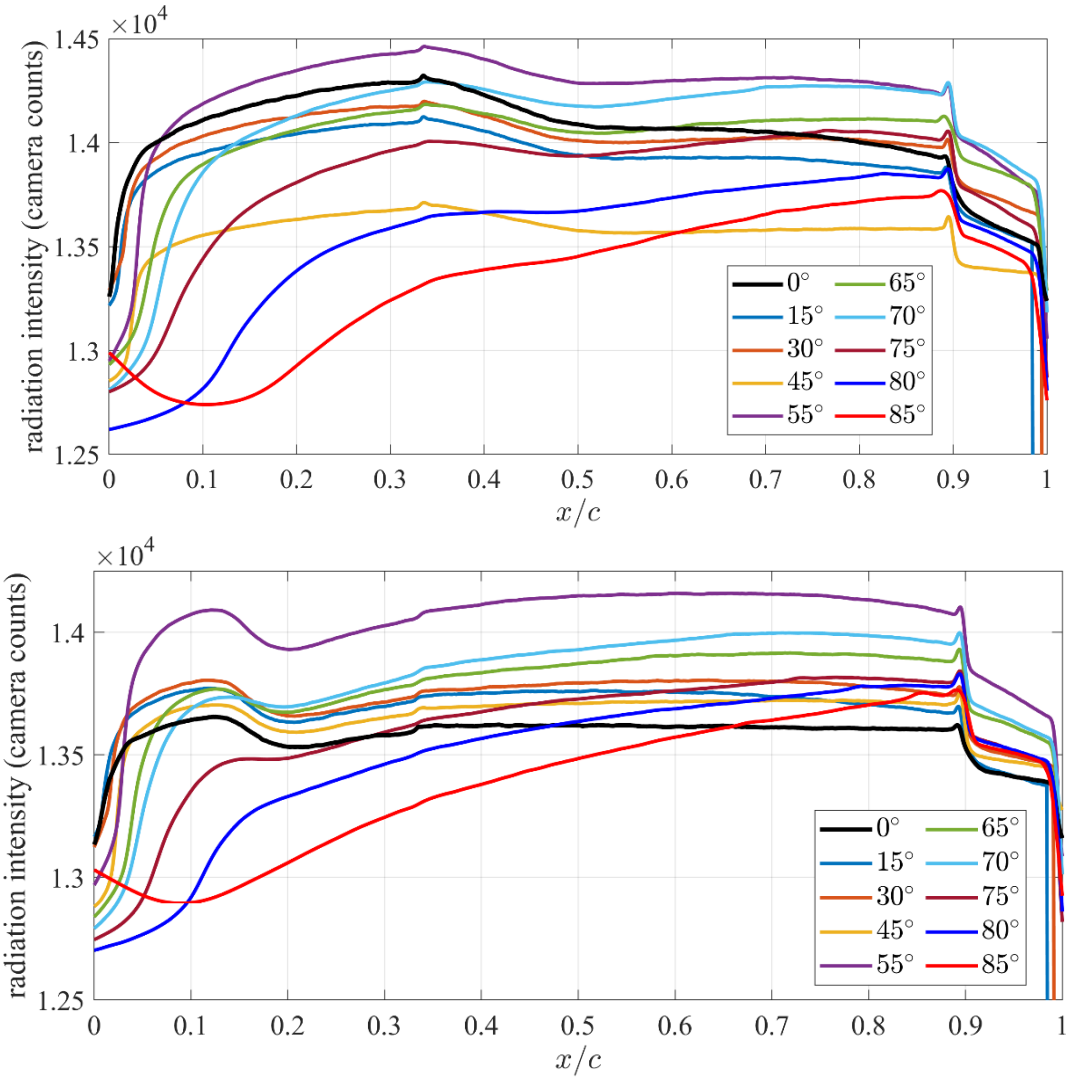

Figure 7: Spanwise averaged and chordwise mapped radiation intensity data after perspective correction for all viewing angles. Top:α=4°, bottom α=5.5°

data to data sets that can be easily analysed to determine the BLT location. For the wind tunnel setting of this study, the accuracy could be enhanced by making use of the available information about the test object and setup geometry, which is however not typically given in a flight test environment.

3.2 Directional Emissivity Correction

The dependence of the emitted radiation on the orientation between surface and sensor is a well-known physical phenomenon that is covered in many materials related to IRT, for example in the relevant AGARDograph [15], where it is detailed how the effect depends also on the specific material choice. If the directional emissivity curves for the tested object are not available, the correction of the directional emissivity effect can be addressed by performing a simple laboratory test. For this study a test has been conducted with a sample of the black vinyl foil, the results of which are shown in Figure 8.

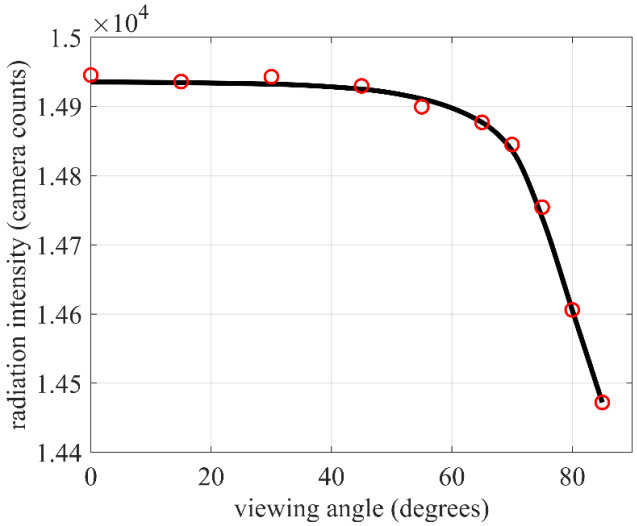

Figure 8: Empirical directional emissivity correction curve. Red circles: laboratory test measurements. Black line: smooth curve fit used for correction.

The test has been conducted in a laboratory environment where the wind tunnel setting (heat lamp and infrared camera distances and positions) have been replicated with a flat plate sample. The measured results seen in Figure 8 correspond well to the expected qualitative behaviour, with a steep drop after exceeding $60°$ between the sensor and the surface normal axes. Quantitatively, the value of the emissivity itself is of no direct interest, since the wind tunnel measurements were performed without temperature calibration. As such, the empirical correction curve is applied by multiplying the inverse of the normalized radiation intensity ratio with the measured, perspective-corrected radiation intensity shown in Figure 7, depending on the orientation angle between the surface normal and the principal viewing axis of the camera. This angle is calculated analytically, based on the knowledge about the measurement setup, for each chordwise location on the wing surface and camera orientation. Exemplary results of the effect of the emissivity correction are shown in Figure 9, showing the uncorrected and corrected data for $65°$ and $75°$ camera positions at $\alpha = 4°$ and $\alpha = 5.5°$, respectively. Below $65°$, the effect of the correction is very small, as can be derived from Figure 8. At $65°$, the effects become visible, particularly near the leading edge where the temperature drop is corrected. A secondary effect of the correction is that all data with a local orientation angle above $85°$ gets discarded, which removes erroneous behaviour directly at the leading edge that is an artifact of the perspective correction not considering the local curvature. For $75°$, the effect of the emissivity correction is even more pronounced, and in the shown case it is able to recover the local peak and trough behaviour due to BLT around $x/c = 0.15$. The BLT location is determined for the data sets with and without emissivity correction in the following, to quantify the effects of this particular processing step.

3.3 Boundary Layer Transition Detection

The BLT location is determined with the simplest available quantitative approach, which is the identification of the location with the minimum of the chordwise temperature gradient [15]. A critical step in this analysis is the smoothing of the temperature data, because the calculation of the gradient amplifies the measurement noise. A straightforward data filtering procedure, namely two passes of a moving mean filter with a window size of $x/c = \pm 2\%$ is applied to all data sets. It is shown exemplary in Figure 10 for both α at the viewing angle $0°$, at which the corrected and uncorrected data sets are nearly identical.

When analysing the raw gradient data shown in Figure 10, it is immediately noticeable that the different segments of the wing cause spikes in the gradient signal $x/c = 0.33$ and $x/c = 0.90$. BLT is not expected occur near the trailing edge, as such the data downstream of $x/c = 0.85$ can simply be discarded from the analysis. Similarly, the leading edge data upstream of $x/c = 0.05$ is also not analysed. The spike at the junction around $x/c = 0.35$ is not treated specifically and smoothed by the general data filtering procedure. As visible in Figure 10, the employed simple low-pass filtering approach is sufficient to remove the fluctuations from the signal and identify the BLT location as minimum of the signal. For the shown cases, these locations are $x_{tr}/c = 0.4245$ for $\alpha = 4°$ and

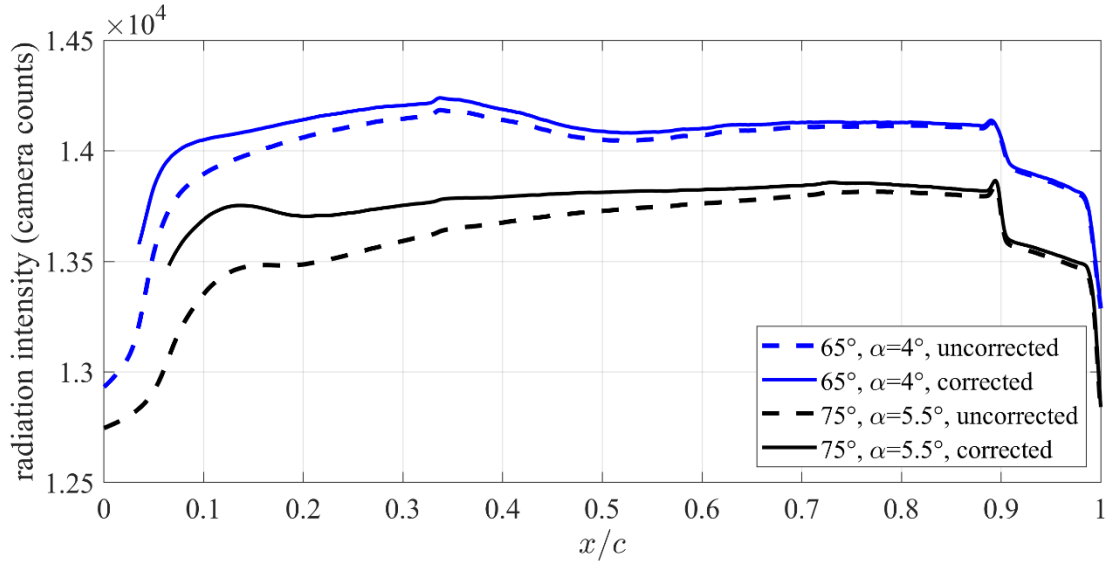

Figure 9: Effect of the directional emissivity correction for two exemplary test cases

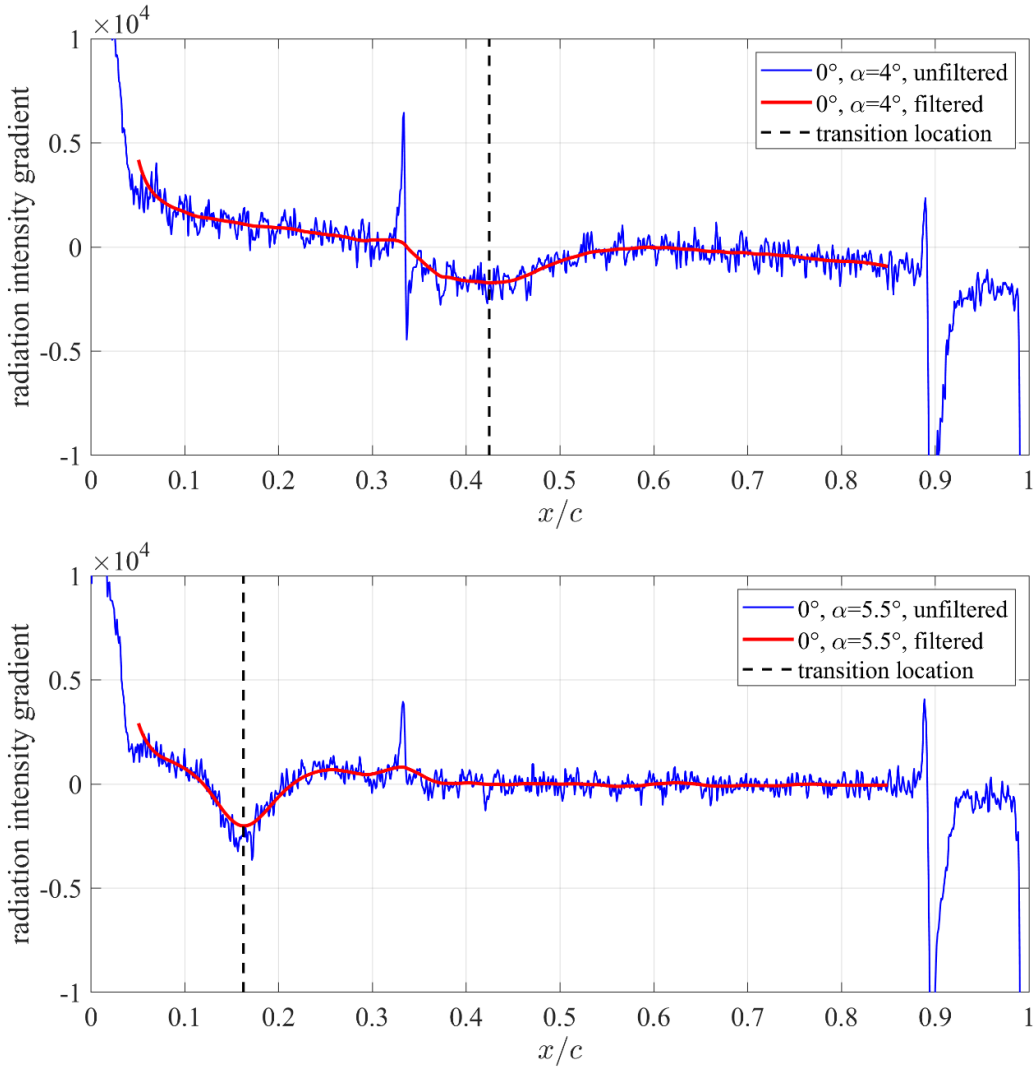

Figure 10: Boundary layer transition location determination by means of the minimum chordwise temperature gradient, including the effect of data smoothing. Top:α=4°, bottom α=5.5°

$x_{tr}/c = 0.1625$ for $\alpha = 5.5°$. These values are considered to be coherent with the XFOIL analysis in section 2.2.

4. RESULTS AND DISCUSSION

The results of the BLT determination for both angles of attack, all viewing angles and both data sets (with and without directional emissivity correction) are shown in Table 1. There is generally a good agreement between the data with and without emissivity correction as well as with increasing orientation angles. However, as the orientation angle approaches the highest values, the BLT location determination based on the minimum of the gradient fails to indicate the correct BLT location. This is the case for all cases at both angles of attack when the orientation angle is $85°$, indicating that BLT measurements at this orientation angle are generally not feasible. For $\alpha = 4°$, the BLT determination works correctly at $80°$ only when the emissivity correction is applied, without the correction it fails. Similarly for $\alpha = 5.5°$, the BLT location determination works at $75°$ only when the emissivity correction is applied, at $80°$ it fails in both cases. This is likely due to the fact the BLT location is further upstream for $\alpha = 5.5°$ and thus affected by the airfoil curvature.

In Figure 11, the same results are visualized graphically by calculating the difference for each data point from the reference value, which is taken as the uncorrected data point at $0°$ camera orientation, for both α, respectively. The difference is given as $\Delta\, x/c$ in percent of the chord length. The graph shows that the majority of data points are within only $\pm 1\%$ of the chordwise location with respect to the reference, which is considered an accurate result. Also the data points where only the corrected results are available are near this range. The outliers, where the BLT determination can be considered as failed are not included in this plot.

Table 1: Boundary layer transition location results

Orient-ation angle	Transition location x_{tr}/c			
	$\alpha = 4°$		$\alpha = 5.5°$	
	No emissivity correction	With emissivity correction	No emissivity correction	With emissivity correction
0°	0.4245	0.4235	0.1625	0.1625
15°	0.4285	0.4285	0.1615	0.1615
30°	0.4295	0.4295	0.1595	0.1595
45°	0.4255	0.4255	0.1645	0.1645
55°	0.4205	0.4205	0.1595	0.1595
65°	0.4385	0.4375	0.1595	0.1575
70°	0.4195	0.4155	0.1675	0.1635
75°	0.4235	0.4155	0.8455	0.1705
80°	0.8505	0.4355	0.8485	0.8475
85°	0.0395	0.7765	0.0405	0.7135

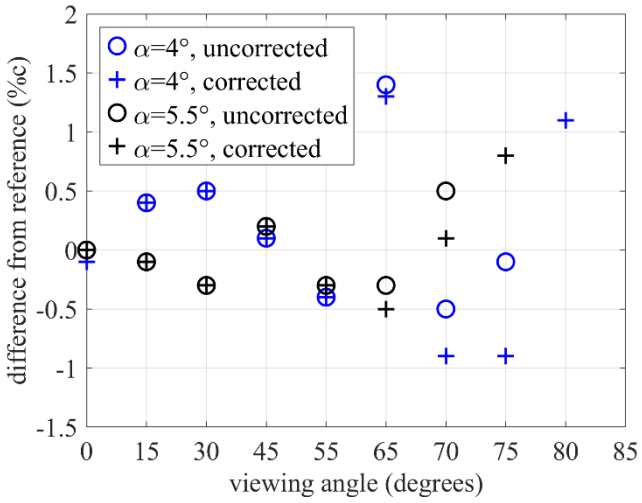

Figure 11: Visualization of the differences in transition location measurement from the 0° viewing angle reference in percent of the chord length.

5. CONCLUSION AND OUTLOOK

This study has shown that the BLT determination based on IRT measurements is relatively robust to the camera orientation angle with respect to the object surface. Angles up to $70°$ between the principal viewing axis of the infrared camera and the surface normal have been demonstrated to work reliably in all cases and confirmed as general best practice.

The implementation of a simple, empirical correction for the directional emissivity effects has been demonstrated to improve the measurement capabilities, allowing angles up to $75°$ and even $80°$ when the BLT location is near the mid-chord. Even under such adverse viewing conditions, the BLT location could be determined reliably within $\pm 1.1\%$ of the chord length using only simple data processing and analysis steps.

The angular limits that were found in this study are very steep angles that would not be typically required for most in-flight measurements. As such, it can be concluded that the infrared camera position for BLT measurements on an aircraft can be freely chosen without considering measurement accuracy limits as long as optical access is warranted.

For future studies, these results will help the design exploration and requirements definition of optical measurement setups for in-flight BLT measurements, especially considering use cases of small-scale experimental aircraft or larger research aircraft with modifications on the wing or tail to quantify the performance of BLT delaying technologies that target drag reduction on future aircraft designs.

References

[1] Schlichting, H., and Gersten, K. (2016). *Boundary-Layer Theory*. Springer. https://doi.org/10.1007/978-3-662-52919-5

[2] Astarita, T., and Carlomagno, G. M. (2012). *Infrared thermography for thermo-fluid-dynamics*. Springer. https://doi.org/10.1007/978-3-642-29508-9

[3] Voogt, N. (1996). Flight Testing a Fokker 100 Test Aircraft with Laminar Flow Glove. *Proc. Second European Forum on Laminar Flow Technology* (pp. 2.3–2.14).

[4] Schrauf, G. H. and von Geyr, H. (2020). *Simplified Hybrid Laminar Flow Control for the A320 Fin - Aerodynamic and System Design, First Results*. AIAA Scitech 2020 Forum, 6-10 January 2020, Orlando, FL, United States. https://doi.org/10.2514/6.2020-1536

[5] Schrauf, G. H. and von Geyr, H. (2021). *Simplified Hybrid Laminar Flow Control for the A320 Fin Part 2: Evaluation with the eN -method*. AIAA Scitech 2021 Forum, Virtual Event. https://doi.org/10.2514/6.2021-1305
[6] van Dam, C. P., Shiu, H. J., Banks, D. W., Tracy, R. R. and Chase, J. (2002). In-Flight Visualization of Supersonic Flow Transition Using Infrared Imaging. *Journal of Aircraft, 39(6)*. https://doi.org/10.2514/2.3046
[7] Frederick, M. A., Banks, D. W., Garzon, G. A. and Matisheck, J. R. (2015). Flight tests of a supersonic natural laminar flow airfoil. *Measurement Science and Technology, 26(6), 064003*. https://doi.org/10.1088/0957-0233/26/6/064003
[8] Yang, T., Zhong, H., Chen, Y., Shi, Y., Bai, J., and Qin, F. (2021). Transition prediction and sensitivity analysis for a natural laminar flow wing glove flight experiment. *Chinese Journal of Aeronautics, 34(8), 34–47*. https://doi.org/10.1016/j.cja.2020.12.042
[9] Gibson, T., Soucheleau, B., and Rogers, N. (2021). BLADE - Natural Laminar Flow Flight Testing, 32nd Congress of the ICAS 2021, 6-10 September 2021, Shanghai, China. Paper 0220. https://www.icas.org/icas_archive/ICAS2020/data/papers/ICAS2020_0220_paper.pdf
[10] Wild, J. (2012). Experimental investigation of Mach-and Reynolds-number dependencies of the stall behavior of 2-element and 3-element high-lift wing sections. In *50th AIAA Aerospace Sciences Meeting including the New Horizons Forum and Aerospace Exposition* (p. 108). https://elib.dlr.de/74041/1/AIAA-2012-108-392.pdf
[11] Drela, M. (1989). XFOIL: An Analysis and Design System for Low Reynolds Number Airfoils. In: Mueller, T.J. (eds) Low Reynolds Number Aerodynamics. Lecture Notes in Engineering, vol 54. Springer, Berlin, Heidelberg. https://doi.org/10.1007/978-3-642-84010-4_1
[12] Van Ingen, J. (2008). The eN method for transition prediction. Historical review of work at TU Delft. In *38th Fluid Dynamics Conference and Exhibit* (p. 3830). https://doi.org/10.2514/6.2008-3830
[13] https://www.flir.com/products/a655sc/
[14] Wolf, C. C., Gardner, A. D., and Raffel, M. (2020). Infrared thermography for boundary layer transition measurements. *Measurement Science and Technology*, *31*(11), 112002. https://iopscience.iop.org/article/10.1088/1361-6501/aba070
[15] AGARDograph 300 Flight Test Techniques Series volume 23: Flight Test Measurement Techniques for Laminar Flow. NATO Science and Technology Organization. Edited by D. Fisher, K.H. Horstmann and H. Riedel, 2003.

List of Symbols

c = chord length, m
C_f = skin friction coefficient, -
C_ℓ = lift coefficient, -
N = critical amplification ratio, -
s = span width, m
T_∞ = freestream temperature, $\mathrm{°C}$
U_∞ = freestream velocity, $\mathrm{m/s}$
x_{tr} = transition location, m
α = geometric angle of attack, °

List of Abbreviations

AWT = acoustic wind tunnel
BLT = (laminar-to-turbulent) boundary layer transition
DLR = German Aerospace Centre
DNW = German-Dutch wind tunnels
IRT = infrared thermography
LSB = laminar separation bubble
NL = Netherlands
NLR = Royal Netherlands Aerospace Centre
SFTE = Society of Flight Test Engineers

Acknowledgement

The authors gratefully acknowledge the help of Anna Biancotto and Lennard de Graaf during the preparation and conduction of the wind tunnel experiment. Furthermore, the contribution of Cecilio Ruiz Martínez to the data processing and analysis is gratefully acknowledged.

Funding Statement

This project has received NLR-internal research funding. No external funding sources are reported.